Electric Field Induced Dewetting at Polymer/Polymer Interfaces

Zhiqun Lin, Tobias Kerle, and Thomas P. Russell*

Department of Polymer Science and Engineering, University of Massachusetts, Amherst, Massachusetts 01003

Erik Schäffer and Ullrich Steiner*

Department of Polymer Chemistry, University of Groningen, 9747 AG Groningen, The Netherlands

Received February 27, 2002

ABSTRACT: External electric fields were used to amplify interfacial fluctuations in the air/polymer/polymer system where one polymer dewets the other. Two different hydrodynamic regimes were found as a function of electric field strength. If heterogeneous nucleation leads to the formation of holes before the electrostatically driven instability sets in, the dewetting kinetics is not influenced by the electric field. Stronger electric fields lead to a spinodal electrohydrodynamic instability which causes the formation of polymer columns on top of the second polymer. The rapid column formation leads to a substantial deformation of the lower polymer layer at the column contact line, caused by the high viscous stress concentration there. With time, the deformation of the lower polymer layer is increased by the action of the interfacial electrostatic force. In addition, the analysis of the polymer−polymer interface during the early stage of the instability indicates a slip boundary condition for the upper layer on the liquid substrate.

Introduction

The stability and homogeneity of thin films and multilayer structures are of interest both academically and technologically, for example, in microlithography, coatings, and adhesion.[1−14] If liquid A dewets a solid substrate B, such as a Si wafer, Young's construction shows that the shape of the dewetting droplet depends on the surface energies of the polymer and substrate and the interfacial energy. If the lower substrate is liquid, such as an amorphous polymer above its glass transition temperature, the interface between liquid A and liquid B will be deformed to minimize the interfacial energy between A and B in accordance with the Neuman construction. If a liquid is spread on a surface, it does not wet, and the resulting film is metastable; then, with time, dewetting will occur. de Gennes, Brochard, and Joanny theoretically investigated the dewetting dynamics at the liquid/liquid interface in great detail.[2,3,6]

Lambooy et al.[11] investigated thin PS films on PMMA as a function of the molecular weight of PMMA at 170 °C and qualitatively compared their experimental results to the Brochard theory.[6] By varying the degree of coupling of the flows in the two layers, deformation at the PMMA/PS interface was found to decrease with the increasing PMMA molecular weight or viscosity. Qu et al.[12] examined the dewetting of PS on PMMA at 162 °C and quantitatively compared their experiments with theory. The dewetting velocity scaled inversely with the PS molecular weight, and three growth regimes, as predicted by Brochard et al.,[6] were observed. The earlier theoretical[3,6] and experimental studies[11,12] indicated that the flow of the dewetting liquid A couples into the substrate layer B due to a nonslip boundary condition at the A/B interface, as schematically shown in Figure 1. For a low enough viscosity of the lower liquid layer, the high viscous stresses at the contact line lead to a wave front at the liquid/liquid interface that precedes the dewetting front.

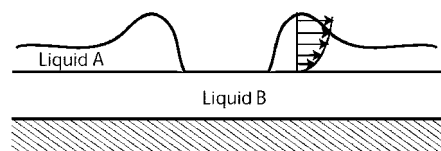All of these studies focused on systems driven dominantly by differences in the interfacial energies. Electric

Figure 1. Dewetting at the liquid−liquid interface. A flow of the dewetting liquid A couples viscously to the substrate layer B at the A/B interface.

fields,[15−26] on the other hand, have been shown to be an effective means of overcoming interfacial interactions to produce highly oriented arrays of nanoscopic structures.[18,19] Electric fields also have been used to induce instabilities at the liquid/air surface of a thin film, producing ordered lateral structures.[22−25] The calculations of Schäffer et al.[22,23] indicated that the instability exhibits a well-defined lateral wavelength that follows a power-law dependence on the applied electric field. Experiments on films between parallel capacitor plates with a well-defined air gap showed good agreement with theory.[22,23] Herminghaus theoretically predicted a dynamical instability of a dielectric layer between conductive media[26] and showed that electrostatic pressure can overcome dispersive forces and amplify surface fluctuations. The more general case of a liquid/liquid bilayer confined between two solid electrodes has been discussed by Lin et al.[24,25] In general, the model calculations show a means by which the amplification of fluctuations at an interface can be used to tune the size scale of self-assembled structures from the micron to submicron level.

Here, a systematic study on the influence of an applied electric field on two interfaces in a polymer bilayer is discussed. One interface is between the two polymer layers whereas the second interface is at the air surface. As in the thin film case, the electrostatic pressure generates columns of polymer comprising the upper layer that extend to the upper electrode surface. However, the flow in the upper layer required to generate the columns, coupled with the flow in the underlying liquid, produces a deformation at the polymer/

Table 1. Material Parameters of the Polymer Used

polymer	mol wt M_w (kDa)	polydispersity (M_w/M_n)	dielectric constant[25] ϵ	viscosity[a] η (kPa s)	surface tension γ (mN/m)	interfacial tension $\gamma_{PMMA-PS}$ (mN/m)
PMMA	27	1.11	5.24	0.3	28.9	
PMMA	95	1.04		13		1.1
PS	96	1.04	2.95	13	27.8	

[a] At 170 °C, extrapolated from ref 30.

Table 2. Sample List

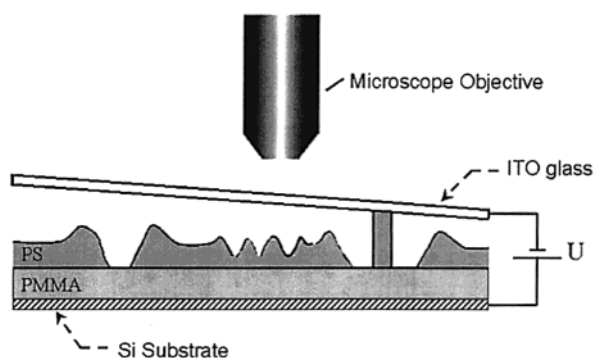| sample no.	polymers	M_w (kDa)	layer thickness (nm)	average electrode spacing (μm)	applied voltage (V)	shown in Figure
1	PMMA/PS	95/96	228/284	1.7	0	4, 5
2	PMMA/PS	95/96	228/284	1.7	30	3, 5, 6, 7, 8
3	PMMA/PS	95/96	228/284	1.7	60	5, 8
4	PMMA/PS	95/96	228/284	1.9	30	8
5	PMMA/PS	95/96	570/284	2.1	60	8 inset
6	PMMA/PS	95/96	570/284	2.5	60	8 inset
7	PMMA/PS	95/96	570/284	2.8	60	8 inset
8	PMMA/PS	27/96	182/284	2.1	0	5
9	PMMA/PS	27/96	182/284	2.1	60	5, 8

Figure 2. Typical sample configuration in this study. The air/polystyrene (PS)/poly(methyl methacrylate) (PMMA) system was sandwiched between a highly polished and doped silicon wafer (lower electrode) and an ITO microscope slide (upper electrode). The distance between the two electrodes was controlled by evaporating SiO$_x$ as a spacer (at the edges of the slides on top of the ITO). Typically, the electrode spacing varied by a few micrometers over a lateral distance of approximately 1 cm. The structure formations of the system under an applied electric field (0, 30 and 60 V) was studied by optical microscopy in the reflectance mode. After removal of the top electrode, the sample was imaged by atomic force microscopy.

polymer interface. With time, this deformation is expected to increase, drawn upward along the outside of the primary polymer cylinder by the electrostatic pressure. The extent of this deformation was measured as a function of the ratio of the molecular weights of the two polymers and the electric field.

Experimental Section

Materials. Poly(methyl methacrylate) (PMMA) and polystyrene (PS) were purchased from Polymer Laboratories Ltd. The relevant material parameters of the three polymers are given in Table 1. Conductive indium−tin-oxide (ITO) microscope slides were purchased from Delta Technologies (25 × 50 × 1.1 mm³, $R_s \leq$ 100 Ω).

Sample Preparation. Figure 2 shows the sample configuration used in this study. A thin film of PMMA was spin-coated onto a freshly cleaned Si substrate. The film thickness was 228 nm for PMMA-95K and 182 nm for PMMA-27K. A thin film of PS-96K was spin-coated onto a clean glass slide having a film thickness of 284 nm. The PS film was floated onto a pool of deionized water and transferred onto the PMMA layer to form the PMMA/PS bilayer. This bilayer was then heated to 60 °C under vacuum for 2 days to remove residual water and entrapped air. All film thickness were measured

with a Rudolph Research AutoEL-II ellipsometer using a helium−neon laser (λ = 632.8 nm) at a 70° incidence angle.

A small air gap, controlled by evaporating silicon oxide rails of a specified thickness onto the ITO microscope slides (the upper electrode), was then used to separate the PMMA/PS bilayer from the ITO glass.[24] Typically, the spacing between the electrodes was not constant, but the samples exhibited a wedge geometry (i.e., the height varied by several micrometers over a lateral distance of 1 cm). After annealing at 170 °C under N$_2$ for 1 day at various applied voltages, the samples were quenched to room temperature before removal of the applied field. The experimental parameters of the samples used in the experiments are given in Table 2.

To examine the polymer/polymer interface, the upper PS layer was removed by washing with cyclohexane for 5 h, followed by ultrasonic cleaning in cyclohexane for 30 min. Subsequently, the sample was placed in another cyclohexane bath for 5 h. Finally, the sample was rinsed with deionized water and dried in a vacuum oven at the room temperature.

An experiment was also performed to examine the influence of an applied field on the dewetting velocity and the dynamic contact angle. Here, in situ optical microscopy studies of the PMMA-95K/PS-96K/air system in the absence of an applied field were performed at 170 °C. The dewetting of PS-96K on PMMA-95K was allowed to proceed for 24 h whereupon 60 V was applied for another 24 h.

Optical microscopy (OM) studies were performed in reflection mode using an Olympus BX60 microscope. Atomic force microscopy (AFM) studies were done with a Digital Instruments D3100 scanning force microscope in the tapping mode. Silicon nitride tips on cantilevers (Nanoprobe) with spring constants from 29.3 to 63.9 N/m were used.

Results and Discussion

The sample setup of the air/liquid 1/liquid 2 trilayer is shown in Figure 2. Since the two capacitor plates were not parallel, but varied by several micrometers over a lateral distance of ∼1 cm, several different instabilities of the liquid 1 layer can be observed on the same sample: (1) For very large electrode spacings, the double film was predominately stable, except for isolated dewetting holes. (2) For intermediate electrode spacings, an undulatory instability of the liquid 1 surface with a characteristic wavelength is observed (see Figure 3a, bottom left). (3) At small enough electrode spacings, an electrohydrodynamic instability caused the formation of liquid columns. This instability is accompanied by the dewetting of the liquid 1 on top of liquid 2. Both the nucleated and spinodal instabilities are observed (see Figure 3a center and top right, respectively).
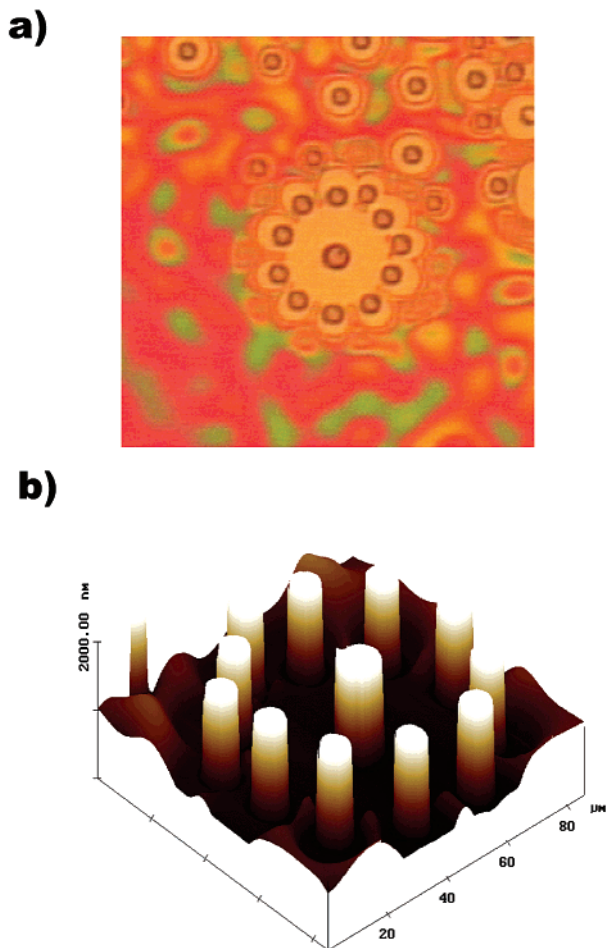
a)

b)

Figure 3. (a) An optical microscope image of sample 2 (30 V) in the configuration shown in Figure 2. The image size was 212×212 μm^2. (b) The corresponding 3D AFM image shows the columns of PS-96K on top of a PMMA-95K layer.

a)

b)

Figure 4. (a) A typical optical micrograph of an intermediate stage of the dewetting process of a thin liquid layer of PS-96K on top of a liquid PMMA-95K substrate (sample 1). (b). A section analysis of AFM images of the dewetting process without an applied electric field. The dotted and the solid curves corresponded to AFM scans before and after removing the PS by rinsing the sample with the selective solvent cyclohexane. Insets are AFM height images before and after removal of the PS layer (left and right).

A summary of the experiments performed in this study is given in Table 2. We start with large capacitor spacings and sequentially discuss the experimentally found morphologies as the electric field is increased. Rather than carrying out a time series with a constant applied field (which limits us to an optical investigation of the sample only), the use of a wedge geometry is an alternative way to observe (in a quasi-static manner) the way how the instability forms with time, since the onset of the instability scales with the sixth power of the electric field in the polymer film.[23]

Dewetting at the Liquid/Liquid Interface at Low Electric Fields. For large plate spacings (Figure 2, left), the influence of external electric fields on the characteristics of the dewetting was investigated. A constant potential was applied between the Si wafer and the ITO glass slide, as schematically shown in Figure 2. Subsequently, the samples were annealed as dewetting and growth of the holes occurred. Two different PMMA/PS bilayers were used, and two different voltages were applied, corresponding to samples 2, 3, and 9 in Table 2. As a reference, identical samples were annealed in the absence of an applied potential (samples 1 and 8).

The optical micrograph in Figure 4a shows two dewetting holes in a thin liquid layer of PS-96K on top of PMMA-95K (sample 1) that are impinging onto one another. With time, the diameters of the isolated holes
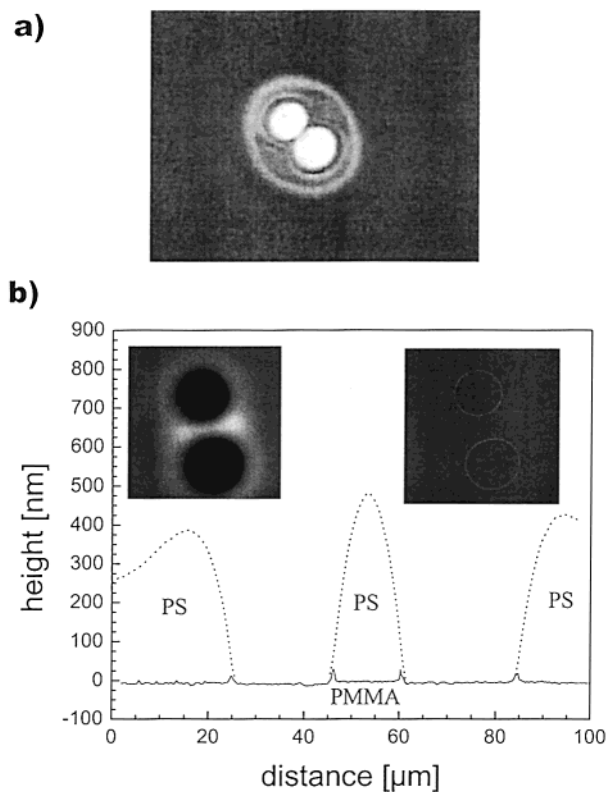
increase, driven by the imbalance of the interfacial and surface energies. The influence of flow in the upper PS layer during dewetting on the lower PMMA layer can be examined by removing the PS layer with cyclohexane, a selective solvent for PS. The inset to the left in Figure 4b shows a tapping mode atomic force microscopy (AFM) image of the sample before removal of PS, whereas the inset on the right shows the same area after removal of the PS with cyclohexane. Superposed line scans of these images are shown in Figure 4b. Deformation of the PMMA/PS interface is evident in the vicinity of the three-phase contact line.

Following the procedure by Lambooy et al.,[11] the extent of the deformation can be characterized by the height h, i.e., peak to baseline distance, and full width at half-maximum (fwhm). Figure 5 shows the variation of h and fwhm as a function of the ratio of the molecular weights of the two polymers. Both h and fwhm increase with an increase in the ratio of the molecular weights. Thus, the coupling of the flows in the two layers increases with a greater mismatch in the molecular weight of PMMA and PS. A comparison of the data in Figure 5 to that obtained by Lambooy et al.,[11] who studied the characteristics of dewetting for the same system, shows reasonable agreement for the functional dependency of the height. However, differences are seen in the full width at half-maximum (fwhm). While the general trend is the same, the data obtained by Lambooy et al.[11] are consistently lower than the data
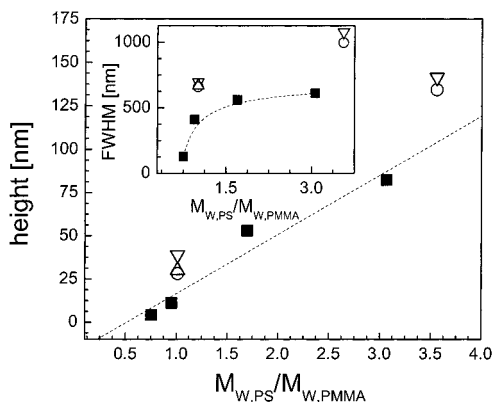
Figure 5. Height (peak to baseline distance) and full width at half-maximum (fwhm) (inset) of the PMMA layer deformation at the PMMA/PS contact line, as a function of the ratio of the molecular weights of the two polymeric liquids. The black squares are the data obtained by analyzing the published measurements of Lambooy et al.[11] The triangle corresponds to sample 2 with 30 V applied. The inverted triangles were obtained with an applied voltage of 60 V (samples 3 and 9). The circles stem from samples with no applied field (samples 1 and 8).

obtained in this study. This difference arises mainly from the greater thickness of the PMMA layers used in this study (182 and 228 nm) as compared to 95 nm used by Lambooy et al.[11,27]

A comparison in Figure 5 of data obtained in the presence or absence of an electric field shows no systematic deviations. For this early stage of dewetting (i.e., for rim heights that are much smaller than the electrode spacing), no time dependence of either the dewetting velocity or the contact angle was observed by in situ optical microscopy. This was confirmed by a control experiment, where the sample was first annealed for 24 h at 160 °C in the absence of an electric field, with subsequent annealing for 24 h with 60 V applied. This is in contrast to electowetting experiments,[28,29] where drop spreading is strongly modified by the electric field. The difference is due to the different electrostatic boundary conditions (a parallel plate capacitor geometry as opposed to a charged conducting liquid on a planar substrate), combined with a small value of the contact angle of the dewetting rim (~2.5°).

More quantitatively, we can estimate the relative strength of the electrostatic force acting at the dewetting rim. The electrostatic pressure at the interface, which operates against the Laplace pressure and viscous forces, can be obtained by taking the derivative of free energy stored in this capacitor system.[22–26] It is given as

$$p_{el,PS/air} = -\frac{U^2}{A}\frac{dC}{dh_{PS}} = \frac{U^2\epsilon_{air}\epsilon_{PS}\epsilon_{PMMA}\epsilon_0}{K^2}\epsilon_{PMMA}(-\epsilon_{PS} + \epsilon_{air}) \quad (1)$$

where $K = \epsilon_{PS}\epsilon_{PMMA}(d - h_{PS} - h_{PMMA}) + \epsilon_{air}\epsilon_{PMMA}h_{PS} + \epsilon_{air}\epsilon_{PS}h_{PMMA})$, and U, ϵ_0, ϵ_{air}, ϵ_{PS}, and ϵ_{PMMA} are the applied voltage, the permittivity in a vacuum, the dielectric constants of air, PS, and PMMA, respectively. d, h_{PS}, and h_{PMMA} are the separation distances between the two electrodes and the film thickness of PS and PMMA, respectively.

This has to be compared with the capillary force per unit length that favors dewetting

$$F_{cap} = \frac{1}{2}\gamma_{PS}(\theta_e{}^2 - \theta^2) \quad (2)$$

θ is the dynamic contact angle and θ_e is the equilibrium contact angle as obtained from Young's equation $\gamma_{PS}\cos(\theta_e) + \gamma_{PS/PMMA} = \gamma_{PMMA}$ with γ_{PS} and γ_{PMMA} the PS and PMMA surface tensions and $\gamma_{PS/PMMA}$ the PMMA/PS interfacial tension. The viscous force that retards dewetting is given by

$$F_{visc} \sim \eta_{PS}\frac{v_d}{\theta} = \gamma_{PS}\theta^2 \quad (3)$$

where we have used the relation for the dewetting velocity v_d given by Tanner's law:[1] $v_d \sim \gamma_{PS}\theta^3/\eta_{PS}$, with η_{PS} the viscosity of PS.

With a dynamic contact angle of $\theta \approx 2.5°$ determined from Figure 4 and $\theta_e \approx 5°$, we find from eq 2 $F_{cap} \approx 2.4 \times 10^{-1}$ N/m. The retarding viscous force is (eq 3) $F_{visc} \sim 1 \times 10^{-1}$ N/m. The electrostatic force per unit length is obtained by integrating eq 1 over the cross section of the PS rim. $F_{el,PS/air} \approx \int P_{el,PS/air} dh_{PS} \sim 1 \times 10^{-1}$ N/m. All three forces are comparable and determine the spreading kinetics in the parameter regime of Figure 3. As opposed to the other two terms, $F_{el,PS/air}$ exhibits a strong variation with d ($\sim 1/d$) and falls off rapidly for $h_{PS} + h_{PMMA} \ll d$. This explains the morphology of the PS layer in Figure 3, which shows the crossover, where $F_{el,PS/air}$ becomes dominant. Because of the strongly nonlinear d dependence, $F_{el,PS/air}$ plays only a negligible role in the dewetting of PS on PMMA and modifies neither the contact angle nor the dewetting kinetics, if d is larger than a critical value. If, on the other hand, d is smaller than this critical value, it dominates the force balance, and columns are formed by the rapid acceleration of PS toward the top electrode. Figure 3 shows a stage in the PS dewetting, where the PS rim height has grown to 400 nm. At this specific stage, the crossover value of d lies at ~ 1.7 μm.

Electrohydrodynamic Interfacial Instabilities. For a decreased plate spacing, corresponding to an increased field in the three layers, the electrostatic pressure at the liquid−air surface is strong enough to destabilize the film surface for the experimental conditions (temperature, annealing time) used here. Similar to the polymer−air bilayer system,[22,23] an undulation with a characteristic wavelength is observed.

The influence of the growth of surface fluctuations and column formation in the upper PS layer on the underlying PMMA layer can be seen by selective removal of the PS layer with cyclohexane. Shown in Figure 6a is an AFM image of the PS surface at an early stage of the growth of fluctuations. A line scan of the surface is shown in Figure 6b where substantial growth in the surface fluctuations is evident with a characteristic period of ~ 35 μm and an amplitude of ~ 0.1 μm. However, after removing the PS layer with cyclohexane, a line scan of the PMMA surface, corresponding to the interface between the PS and PMMA, is featureless. Consequently, the PS/air interface deforms much more readily than the PMMA/PS interface.

Qualitatively, the PS/air surface is expected to deform much more readily than the PMMA/PS interface, since the dielectric contrast between PS and air is much larger compared to the PMMA/PS interface and the
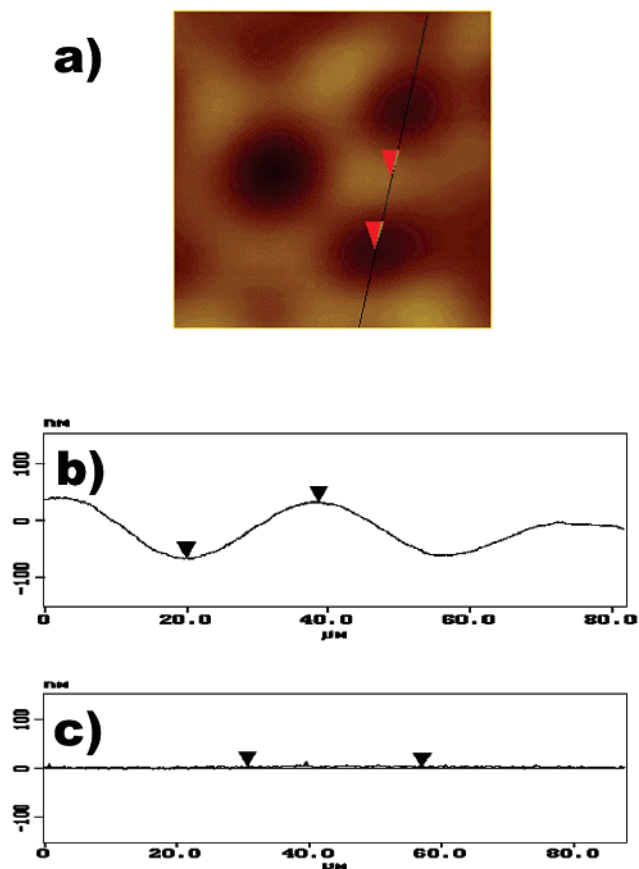
Figure 6. (a) A typical AFM image of the early stages of the instability, corresponding to Figure 3 bottom left (sample 2, 30 V). The section analyses of the image before and after removal of the upper PS layer by cyclohexane are given in (b) and (c), respectively.

viscous damping for the deformation of a free surface is much lower than of a polymer−polymer interface. On the other hand the PS/PMMA interfacial tension is lower, facilitating interfacial deformation.[24] In the presence of an electric field, both interfaces are expected to become unstable. To obtain more quantitative information on the instabilities of the two interfaces, it is instructive to compare the characteristic times at which the instabilities occur. For the PS/air interface, we have the dispersion relation for the mode spectrum[23] q

$$\frac{1}{\tau_{PS/air}} = -\frac{h_{PS}^{3}}{3\eta_{PS}}\left(\gamma_{PS/air}q^{4} + \frac{\partial p_{el,PS/air}}{\partial h_{PS}}q^{2}\right) \quad (4)$$

For the PMMA/PS interface, the equivalent relation is[24]

$$\frac{1}{\tau_{PS/PMMA}} =$$
$$-\frac{(h_{PS}h_{PMMA})^{3/2}}{3C(\eta)}\left(\gamma_{PMMA/PS}q^{4} + \frac{\partial P_{el,PS/PMMA}}{\partial h_{PMMA}}q^{2}\right) \quad (5)$$

$C(\eta)$ is a function of the viscosities and film thicknesses of the PS and PMMA layers.[24] In the limit $\eta_{PMMA} \approx \eta_{PS}$ and $h_{PS} \approx h_{PMMA}$, $C(\eta) \approx 8\eta_{PS}$. The electrostatic pressure

acting at the PS surface is given by eq 1. Similarly, the pressure at the PMMA/PS interface can be given as

$$P_{el,PS/PMMA} = -\frac{U^{2}}{A}\frac{dC}{dh_{PMMA}} =$$
$$\frac{U^{2}\epsilon_{air}\epsilon_{PS}\epsilon_{PMMA}\epsilon_{0}}{K^{2}}\epsilon_{air}(-\epsilon_{PMMA} + \epsilon_{PS}) \quad (6)$$

where K is the same as in eq 1.

Maximizing $1/\tau$ in eqs 4 and 5 with respect to q yields the most unstable mode and the maximal growth rates.[23,24] Using the experimental parameters from Tables 1 and 2, we have $\tau_{PS/air} \approx 6$ h, as found in Figure 6, and $\tau_{PS/PMMA} \approx 16$ days. Note that eq 5 assumes a nonslip boundary condition at the PMMA/PS interface. Perfect slip at the PMMA/PS boundary reduces $\tau_{PMMA/PS}$ by almost a factor of 8 ($C(\eta) \approx \eta_{PS}$). For both boundary conditions, however, $\tau_{PS/air}$ is considerably smaller compares to $\tau_{PMMA/PS}$. The instability of the polymer−air interface is therefore expected to preempt the instability at the polymer−polymer interface, in agreement with our experimental observations.

We now turn our attention to the lack of hydrodynamic deformation of the PMMA/PS interface. In an earlier paper,[24] we investigated the electrohydrodynamic instability of liquid polymer/polymer interfaces. There, we have assumed the hydrodynamic flow profiles in the two polymers to be viscously coupled. Here, in the case of polymers with comparable viscosities, this implies a Poiseulle-type flow profile extending from the solid substrate to the air interface, which is nearly continuous at the polymer−polymer interface. In such a model, the polymer−polymer interface is expected to mirror the undulations of the PS/air surface. In contrast, the results in Figure 6 show an undeformed PMMA layer. Since PMMA is liquid and cannot sustain a shear stress, our experimental observations are direct evidence for interfacial slip at the polymer−polymer interface.

Interfacial slip between two polymers is not unusual. Because of their incompatibility, the interfacial interpenetration of PS and PMMA is ∼5 nm.[31] In particular, PS and PMMA chains are not expected to be entangled at the interface. In addition, liquid surfaces are more homogeneous compared to solid substrates, in terms of both their chemical composition and surface roughness. Slip at a polymer interface was previously reported by Reiter and Khanna.[32] In a very recent study, Wang et al.[27] found evidence for slippage when studying the dewetting of PS on PMMA. Slippage could also explain the accelerated electrohydrodynamic instability of polymer−polymer interfaces in our earlier study.[24]

Electric Field Induced Structure Formation. For even smaller values of the electrode spacing (Figure 2, right), the amplification of surface waves discussed in the previous paragraph led to the formation of PS columns that spanned from the surface of the PMMA film to the top electrode. Evidence for both nucleated and spinodal instabilities was found. In the upper right-hand section of Figure 3a, columns of PS are evident that are surrounded by a dewetting zone that propagates away from the columns. The structure in the center of the dewetting micrograph consists of an initial column (primary cylinder) that was heterogeneously nucleated early in the experiment. As the dewetting rim grew in size and height, fluctuations with a characteristic spac-
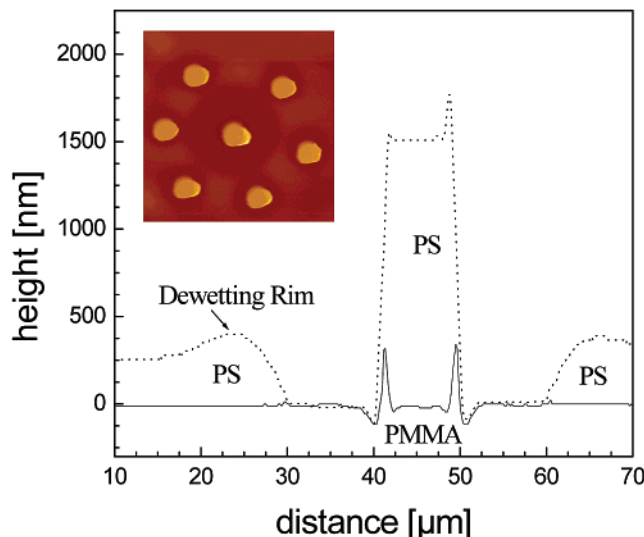
Figure 7. Deformation of the PMMA-95K/PS-96K interface (sample 2 with 30 V applied) caused by the flow of PS into the primary cylinder. The main graph shows superposed line scans of the PS/air (dotted line) and PMMA/PS (full line) interfaces. The inset is the corresponding AFM height image.

Figure 8. Deformation of height under the dewetting rim as a function of the ratio of the molecular weights of the PS and PMMA from Lambooy et al.[11] (black squares) and our experiments (gray area). The triangles are the deformations observed for the PMMA-95K/PS-96K system with 30 V applied (▲, sample 2; △, sample 4), and the inverted triangles were obtained with 60 V applied for PMMA-95K/PS-96K (sample 3) and PMMA-27K/PS-96K (sample 9). The inset shows the deformation of height as a function of separation distance of the electrodes, d, for the PMMA-95K/PS-96K bilayer at 60 V applied field (samples 5−7).

ing were amplified and grew into regularly spaced columns (secondary cylinders). Each secondary column was then surrounded by its own dewetting zone. As discussed above, there is no influence of the electric field on the interfacial structure at the dewetting front. However, as PS dewets the PMMA, PS accumulates in the dewetting rim, changing the position of the PS/air interface locally. This creates an instability along the rim which, in turn, leads to the formation of secondary cylinders. An AFM image of the structure in the center of the optical micrograph is shown in Figure 3b. This image more clearly shows the columnar shape of these features that are ~1.5 μm in height with a diameter of ~10 μm. It should be noted that the central column is much larger than the column formed on the dewetting rim. Similar to the nucleated instability, the columns formed by a spinodal process (Figure 3, top right) are each surrounded by a dewetting zone.

These findings are reminiscent of the electric field induced structures formed with a single polymer film on a solid substrate,[22] with two main differences. First, the dewetting around the PS columns on the PMMA film is much more pronounced compared to the structure formation of PS on a silicon substrate.[22] Second, the PMMA surface, which plays the role of the substrate here, is significantly deformed at the PS−PMMA-air contact line. The greater amount of dewetting is presumably due to the higher negative spreading coefficient for PS on PMMA, compared to a silicon wafer; PS wets clean silicon wafers (with a native oxide layer) but only partially wets PMMA.

The dewetting of a liquid on a liquid substrate results in the deformation of the contact line, since the liquid substrate can not sustain the high shear stresses that build up at the contact line. In addition, the electrostatic forces cause a secondary instability at the PMMA−air surface that is revealed once the PS columns have formed. To analyze the deformation of the liquid/liquid interface caused by the flow into the primary cylinders, the line scans of PS/air and PMMA/PS interfaces, after removal of the upper PS layer, were overlaid. Shown in the inset of Figure 7 is an AFM image of the PS surface.
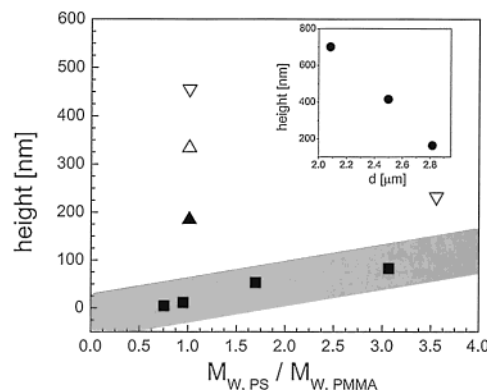
Here, the initial column formed is in the center, surrounded by a ring of columns formed on the dewetting rim. The dashed line in the data shows a line scan across the primary cylinder. The height of the column is ~1.5 μm with a diameter of ~10 μm. After removal of the PS layer by rinsing with cyclohexane, the line scan shown by the solid line was obtained. The two scans were overlaid by normalizing the height at the exposed PMMA layer surrounding the column. Salient features of these data are the three phase contact line located ~10 μm around the column, the dewetting rim, and the deformation of PMMA/PS interface induced by the formation of the column. Surrounding the column is a depression of the PMMA underlayer due to the coupling of flow between the two layers. At the edges of the columns, the underlying PMMA layer is substantially deformed. The extent of this deformation is a direct consequence of the flow of the PS into columns that couples into the underlying PMMA through the interface. In the case shown, this underlying rim at the PS and PMMA interface is ~400 nm in height. The magnitude of the deformation at this buried interface was found to depend on the ratio of the molecular weight of the PS and PMMA.

Shown in Figure 8 is the height of the deformation of the primary cylinder at the PMMA/PS interface under the PS columns as a function of the ratio of PS and PMMA molecular weights. Shown also in this plot are the data of Lambooy et al.[11] obtained by dewetting PS on PMMA in the absence of an applied field. As seen, as this ratio increases or as the mobility of PMMA increases in comparison to that of PS, the extent of deformation at the PMMA/PS interface increases. In addition, for a given ratio of molecular weights, as the applied field strength increases by increasing the applied voltage while keeping the separation distance, d, between two electrode fixed or by decreasing d while keeping the applied voltage fixed (inset in Figure 8), the magnitude of the deformation increases.

Since the time constants for either the PMMA/PS interface or the exposed PMMA surface to become unstable are much larger compared to the initial instability of the PS surface, the contact line deforma-

tion of the PMMA under the cylinders is a secondary process that builds up once the PS columns have formed. It is due to two effects. Initially, it is caused by the hydrodynamic deformation of the PMMA/PS/air contact line, similar to the generic dewetting process of Figure 5. While regular dewetting proceeds at a constant and slow speed (or as a weak power law, in the case of a slip boundary condition[32]), the electrohydrodynamic instability proceeds much more rapidly. The initial undulations seen in Figure 3 (bottom left) are exponentially amplified, leading to a very rapid formation of the columns.[24] This leads to a fast motion of the contact line and, therefore, to a much higher viscous stress concentration there. As a consequence, the liquid PMMA substrate is deformed to a much greater extent than in standard dewetting, as is observed here. This can be seen in the cross-sectional scan in Figure 7, where clearly more PS has been displaced into the electrohydrodynamically formed PS column than into the dewetted PS rims.

Once the primary PS columns have formed (and along with it the PMMA contact line deformation), a secondary electrohydrodynamic instability sets in. The electrostatic forces that act on the PMMA−air surface are much larger than those on the PMMA/PS interface. They are maximal at the location of the PMMA/PS contact line, where the local PMMA film height is largest. With time, the PMMA can be drawn up on the outside of the PS columns forming annuli around the existing PS columns with a suitable field strength and combination of viscosities of PS and PMMA. The relative role the two processes play in the PMMA contact line deformation will be addressed in a forthcoming publication.

Conclusions

We have studied the electrohydrodynamically driven amplification of surface capillary waves of a bilayer comprising of two incompatible polymers. Surprisingly, a minor variation of one of the experimental parameters, the electric field in the three layers (which was varied by changing the electrode spacing by a few percent), results in two distinct hydrodynamic regimes. For low enough electric fields, holes are heterogeneously nucleated in the top polymer layer (PS) which then dewets the liquid substrate, PMMA. This dewetting process is only marginally modified by the electric field. If the electric field is increased (by slightly decreasing the electrode spacing), the buildup of electrostatically amplified surface waves preempts heterogeneous nucleation, resulting in the formation of columns that span from the PMMA to the upper electrode. In this case, the dominant driving force is caused by the electric field. Apart from the different force balance that characterizes the two regimes, they are very different in terms of their hydrodynamics. While the slow paced motion of the contact line during dewetting causes only a small deformation of the PMMA underlayer, the much faster collective motion of the electrohydrodynamic instability leads to high shear stresses and, therefore, to a substantial deformation of the PMMA/PS contact line. With time, PMMA is drawn further upward on the outside of the PS columns by the electric field. Studies of the deformation of the PMMA/PS interface during the early stage of the electrically driven spinodal instability of the PS surface allow us to deduce the hydrodynamic coupling of the two layers. The fact that the PMMA layer

does not participate in the instability indicates the presence of slip at this interface.

Both results indicate that the present experiments may be useful in obtaining quantitative information on liquid−liquid spreading and dewetting. As opposed to dewetting in the absence of an electric field, an applied voltage may be useful as an additional, freely variable external parameter that alters both the force balance and the hydrodynamics. With a suitable (presently unavailable) model, such experiments may yield valuable (and technologically important) insight into the contact line dynamics at the liquid−liquid boundary. In addition, the study of the liquid−liquid interface in the presence of a spinodal electrohydrodynamic instability (rather than rheological studies) may reveal more direct information about slip boundary conditions between incompatible liquids.

References and Notes

(1) Tanner, L. H. *J. Phys. D: Appl. Phys.* **1979**, *12*, 1473.
(2) de Gennes, P. G. *Rev. Mod. Phys.* **1985**, *57*, 827.
(3) Joanny, F. *Phys. Chem. Hydrodyn.* **1987**, *9*, 183.
(4) Brochard-Wyart, F.; Debregeas, G.; de Gennes, P. G. *Colloid Polym. Sci.* **1996**, *274*, 70.
(5) Brochard-Wyart, F.; Daillant, J. *Can. J. Phys.* **1990**, *68*, 1084.
(6) Brochard-Wyart, F.; Martin, P.; Redon, C. *Langmuir* **1993**, *9*, 3682.
(7) Buguin, A.; Vovelle, L.; Brochard-Wyart, F. *Phys. Rev. Lett.* **1999**, *83*, 1183.
(8) Xie, R.; Karim, A.; Douglas, J. F.; Han, C. C.; Weiss, R. A. *Phys. Rev. Lett.* **1998**, *81*, 1251.
(9) Reiter, G. *Phys. Rev. Lett.* **1992**, *68*, 75.
(10) Reiter, G.; Sharma, A.; Casoli, A.; David, M. D.; Khanna, R.; Auroy, P. *Europhys. Lett.* **1999**, *46*, 512.
(11) Lambooy, P.; Phelan, K. C.; Haugg, O.; Krausch, G. *Phys. Rev. Lett.* **1996**, *76*, 1110.
(12) Qu, S.; Clarke, C. J.; Liu, Y.; Rafailovich, M. H.; Sokolov, J.; Phelan, K. C.; Krausch, G. *Macromolecules* **1997**, *30*, 3640.
(13) Kerle, T.; Yerushalmi-Rozen, R.; Klein, J.; Fetters, L. J. *Europhys. Lett.* **1998**, *44b*, 484.
(14) Wu, S. *Polymer Interface and Adhesion*; Marcel Dekker: New York, 1982.
(15) Morkved, T. L.; Lu, M.; Urbas, A. M.; Ehrichs, E. E.; Jaeger, H. M.; Mansky, P.; Russell, T. P. *Science* **1996**, *273*, 931.
(16) Mansky, P.; DeRouchey, J.; Russell, T. P.; Mays, J.; Pitsikalis, M.; Morkved, T. Jaeger, H. *Macromolecules* **1998**, *31*, 4399.
(17) Amundson, K.; Helfand, E.; Davis, D. D.; Quan, X.; Patel, S. S. *Macromolecules* **1991**, *24*, 6546. Amundson, K.; Helfand, E.; Quan, X.; Smith, S. D. *Macromolecules* **1993**, *26*, 2698. Amundson, K.; Helfand, E.; Quan, X.; Hudson, S. D.; Smith, S. D. *Macromolecules* **1994**, *27*, 6659.
(18) Thurn-Albrecht, T.; Steiner, R.; DeRouchey, J.; Stafford, C. M.; Huang, E.; Bal, M.; Tuominen, M.; Hawker, C. J.; Russell, T. P. *Adv. Mater.* **2000**, *12*, 787.
(19) Thurn-Albrecht, T.; Schotter, J.; Kastle, G. A.; Emley, N.; Shibauchi, T.; Krusin-Elbaum, L.; Guarini, K.; Black, C. T.; Tuominen, M. T.; Russell, T. P. *Science* **2000**, *290*, 2129.
(20) Pelrine, R.; Kornbluh, R.; Pei, Q. *Science* **2000**, *287*, 836.
(21) Onuki, A. *Physica A* **1995**, *217*, 38.
(22) Schäffer, E.; Thurn-Albrecht, T.; Russell, T. P.; Steiner, U. *Nature (London)* **2000**, *403*, 874.
(23) Schäffer, E.; Thurn-Albrecht, T.; Russell, T. P.; Steiner, U. *Europhys. Lett.* **2001**, *53*, 518.
(24) Lin, Z.; Kerle, T.; Baker, S. M.; Hoagland, D. A.; Schaffer, E.; Steiner, U.; Russell, T. P. *J. Chem. Phys.* **2001**, *114*, 2377.
(25) Lin, Z.; Kerle, T.; Russell, T. P.; Schaffer, E.; Steiner, U. *Macromolecules* **2002**, *35*, 3971.

(26) Herminghaus, S. *Phys. Rev. Lett.* **1999**, *83*, 2359.
(27) Wang, C.; Krausch, G.; Geoghegan, M. *Langmuir* **2001**, *17*, 2928.
(28) Blake, T. D.; Clarke, A.; Stattersfield, E. H. *Langmuir* **2000**, *16*, 2928.
(29) Oddershede, L.; Nagel, S. *Phys. Rev. Lett.* **2000**, *83*, 1234.
(30) Fox, T. G.; Flory, P. J. *J. Polym. Sci.* **1954**, *14*, 315.
(31) Anastasiadis, S. H.; Russell, T. P.; Satija, S. K.; Majkrzak, C. F. *Phys. Rev. Lett.* **1989**, *62*, 1852.
(32) Reiter, G.; Khanna, R. *Phys. Rev. Lett.* **2000**, *85*, 2753.